




An Improved Low Rank and Sparse Matrix Decomposition-Based Anomaly Target Detection Algorithm for Hyperspectral Imagery

Yan Zhang , Yanguo Fan , Mingming Xu , *Member, IEEE*, Wei Li , *Senior Member, IEEE*, Guangyu Zhang, Li Liu, and Dingfeng Yu

Abstract—Anomaly target detection has been a hotspot of the hyperspectral imagery (HSI) processing in recent decades. One of the key research points in the HSI anomaly detection is the accurate descriptions of the background and anomaly targets. Considering this point, we propose a novel anomaly target detector in this article. Improving upon the low-rank and sparse matrix decomposition (LRaSMD) approach, the proposed method assumes that the low-rank component can be described as the parts-based representation. Parts refer to the various ground objects in HSI. A new update rule of the low-rank component and sparse component is proposed. The proposed approach can be divided into three main steps: first, further refining the low-rank component in the LRaSMD model as the parts-based representation. Then, the HSI is decomposed as three parts: the product of the basis matrix and coefficient matrix, sparse matrix, and noise. Second, the basis vectors matrix, coefficient matrix, and sparse matrix are solved by the new update rules. Third, since the anomaly targets exist in the sparse matrix, the sparse matrix is thus employed to detect the anomaly targets. The experiments implemented for five data sets demonstrate that the proposed algorithm achieved a better performance than the traditional algorithms.

Index Terms—Anomaly target detection, hyperspectral imagery (HSI), low rank, matrix decomposition, parts-based, sparseness.

I. INTRODUCTION

HYPERSPECTRAL imagery (HSI) has a high spectral resolution. Therefore, it contains abundant and detailed

Manuscript received December 10, 2019; revised February 23, 2020 and April 2, 2020; accepted May 3, 2020. Date of publication May 28, 2020; date of current version June 11, 2020. This work was supported in part by the National Key Research and Development Program of China under Grant 2017YFC1405600, in part by the National Natural Science Foundation of China under Grant 61701542, in part by the Key Research and Development Program of Shandong Province under Grant 2019GHY112017, and in part by the Postgraduate Innovation Project Funding Project under Grant YCX2019009. (*Corresponding authors: Yanguo Fan; Mingming Xu.*)

Yan Zhang, Yanguo Fan, Mingming Xu, and Guangyu Zhang are with the College of Oceanography and Space Informatics, China University of Petroleum (East China), Qingdao 266580, China (e-mail: rs_zhangyan@163.com; ygf@upc.edu.cn; xumingming900405@126.com; zhangguang@163.com).

Wei Li is with the School of Information and Electronics, Beijing Institute of Technology, Beijing 100081, China (e-mail: liwei089@ieee.org).

Li Liu is with the China Petroleum Engineering and Construction Corporation Xinjiang Petroleum Engineering Company Ltd., Karamay 834000, China (e-mail: liuli-xj@cnpc.com.cn).

Dingfeng Yu is with the Institute of Oceanographic Instrumentation, Qilu University of Technology (Shandong Academy of Sciences), Jinan 250353, China (e-mail: dfyucsas@163.com).

Digital Object Identifier 10.1109/JSTARS.2020.2994340

spectral information of ground objects [1]–[3]. This advantage greatly improves the capabilities in distinguishing the ground objects, even for the minor differences between different objects [4]–[6]. In that case, the target detection and classification using HSI can be more effective than using multispectral imagery. The former application aims at extracting the objects of interest from a specific scene. The conventional target detectors are usually designed as the matching filter and subspace projection detector, such as the adaptive matched filter [7], spectral angle matching [8], and orthogonal subspace projection [9]. However, the target spectra information is not always available. Therefore, the anomaly target detection is suitable when the target spectra are absent. The anomaly detectors use the characteristics of the anomaly target instead of prior target knowledge to implement the detection processing.

The anomaly target detection focuses on extracting the objects from the original HIS. The spectra of the anomaly targets are distinctly different from the typical background. In the anomaly target detection for the HSI, there are two key problems: first, the description of the anomaly target and background, and second, the separation of the anomaly target and background. The description of the anomaly target and background is the first step and important step in the anomaly target detection for the HSI. A well-designed description model should account for the most fundamental difference between the anomaly target and background, thereby clearly delineate them.

In the mainstream approaches, many anomaly detection algorithms have focused more on the background statistical information estimation. The Reed–Xiaoli detector (RXD) [10] is considered as the benchmark algorithm of the anomaly target detection and it is a typical detector using the background statistical information estimation. In RXD, the estimated background covariance matrix and mean value are utilized to describe the background. Thus, the accuracy of the background covariance matrix can greatly affect the detection performance of RXD. Some algorithms have subsequently been proposed to solve this problem. For instance, a locally adaptive iterative RXD [11] uses the last time results of RXD to update the background information. The blocked adaptive computationally efficient outlier nominators (BACON) [12] combine the iteration strategy with the original RXD to improve the detection performance. In order to reduce the influence of the anomaly target on the background information, the principal component corresponding to

the larger eigenvalue is removed in the subspace RXD (SSRX) [13]. In summary, almost all RXD-based improved algorithms remove the suspected anomaly target to obtain the accurate background information. Although the above-mentioned algorithms can solve the inaccuracy problem of the background information to an extent, the lower order statistical information still had limitations in accurately describing the background. Therefore, determining how to model the background and anomaly target accurately is still an important problem in the hyperspectral anomaly detection.

In recent years, the anomaly target detection algorithms based on the low rank and sparse matrix decomposition (LRaSMD) [14] and sparse representation (SR) [15]–[17] have been increasingly focused upon and widely researched. The main tenet of LRaSMD and SR is that the background of HSI has a low-rank property. The low-rank property of the background means that the background of HSI is composed of limited materials and the pixels of the same material are continuous. Conversely, the anomaly targets have low probabilities and small occupation pixels [18]. Thus, the anomaly targets have a sparse property. The LRaSMD-based algorithms consider that the original HSI can be decomposed as a low-rank matrix, a sparse matrix, and noise. The anomaly targets are included in the sparse matrix. Some LRaSMD-based algorithms have demonstrated a strong detection performance, such as the LRaSMD-based Mahalanobis distance method for hyperspectral anomaly detection [14], a novel low-rank and sparse decomposition [19], Euclidean distance-based LRaSMD (EDLRaSMD) [20], the LRaSMD-based dictionary reconstruction and anomaly extraction framework for hyperspectral anomaly detection (LSDRAD) [21], and so on [22]. The advantages of the LRaSMD-based algorithms can be summarized as follows.

- 1) They can separate the anomaly target and background through their intrinsic properties, which refer to the sparseness of the anomaly target and the low rank of the background.
- 2) The algorithms consider the sparse, the low rank, and noise component flexibly and simultaneously.
- 3) They do not require a sliding window.

Based on these advantages, we chose the LRaSMD model as the basic framework of the description model used in this article. The LRaSMD-based algorithms search for the solutions from holistic versions. Some parts-based characteristics of HSI and the linear relationship between each pixel and basis endmember may be ignored. The parts-based characteristics of HSI can be interpreted as that the HSI is composed of the limited ground objects and each ground object is a “part” of HSI [23]. All pure endmembers of the ground objects can be interpreted as the “parts” of HSI. Although the SR-based algorithms can use some limited dictionary atoms to reconstruct the background and the target, they cannot solve the anomaly target detection due to the lack of a target dictionary. From another perspective, the atoms in the SR-based algorithms are over complete and cannot represent the basic ground object endmember.

The non-negative matrix factorization (NMF) [23] technique is an excellent parts-based representation approach that has been successfully employed in the face recognition, classification [24] as well as target detection [25], [26]. For instance, a novel

hyperspectral anomaly detection based on similarity constrained convex NMF (SC-CNMF) [27] utilizes the improved convex NMF to reconstruct the background, which has presented a great detection performance. The main content of NMF is that the background of the original HSI can learn the parts-based representation that is more consistent with the way that our brain cognizes the objects. We can utilize this advantage of NMF to accurately reconstruct the parts-based representation of the low-rank component. To further improve the accuracy of the reconstructed imagery, some modified NMF algorithms with different constraints have been proposed [28], [29]. In [23], the sparseness constraint largely controlled the factorization speed and restoration accuracy in NMF.

In this article, we propose an improved LRaSMD-based anomaly target detection algorithm for the HSI, called the parts representation-based low rank and sparse matrix decomposition anomaly detector (PRLRaSAD). Herein, the sparse NMF (SNMF) is employed to assist in solving the basis vectors matrix and the coefficient matrix. Once the accuracy of the low-rank component improves, the accuracy of the sparse component will improve simultaneously.

Compared with the traditional LRaSMD-based algorithms, the main contributions of the proposed method are summarized as follows.

- 1) The traditional LRaSMD-based algorithms search matrix factorization results from searching a holistic version, and some linear and parts-based characteristics may be ignored. The proposed method models the background using a linear representation of the basis vectors that can resolve this issue.
- 2) The proposed method separates the decomposition optimization problem into three subproblems: the optimization of the basis vectors matrix, coefficient matrix, and sparse matrix. We can obtain not only the low-rank matrix and sparse matrix but also the basis vector and the corresponding coefficient matrix of the low-rank matrix.

The rest of this article is organized as follows. Section II introduces the basic knowledge of the LRaSMD and SNMF algorithms. Then, Section III presents the proposed algorithm. In Section IV, the experiments, implemented for five data sets, are depicted and discussed. Finally, Section V concludes this article.

II. RELATED WORK

A. Low Rank and Sparse Matrix Decomposition

The low-rank property of the matrix indicates that the columns and rows of the matrix are highly correlated. In the HSI domain, it can be interpreted that the HSI is composed of limited materials and the pixels of the same materials are continuous [30]. Due to the low probability and small occupation of the pixels, the anomaly targets are labeled as the sparse instead of the low-rank property.

Based on the different properties of the ground objects, the model of LRaSMD for HSI is expressed as follows:

$$\mathbf{X} = \mathbf{L} + \mathbf{S} + \mathbf{E} \quad (1)$$

where $\mathbf{X} \in \mathbf{R}^{b \times n}$ (b is the number of the spectral bands and n is the number of the pixels in HSI, \mathbf{L} is the low-rank matrix, \mathbf{S} is the sparse matrix that contains the anomaly targets, and \mathbf{E} is the noise.

To find an optimal solution of (1), the decomposition error minimization objective function is constructed. The rank of \mathbf{L} and the sparseness of \mathbf{S} also are controlled during the search for the solution of (1). Therefore, the problem is converted as follows:

$$\begin{aligned} \min \|\mathbf{X} - \mathbf{L} - \mathbf{S}\|_F^2 \\ \text{s.t. rank}(\mathbf{L}) \leq k, \text{card}(\mathbf{S}) \leq rn \end{aligned} \quad (2)$$

where k is the upper bound rank number of matrix \mathbf{L} and rn reflects the sparseness degree of matrix \mathbf{S} .

The optimization problem of (2) can be converted into two subproblems. Then, (2) is replaced by

$$\begin{aligned} \mathbf{L}_t &= \arg \min_{\text{rank}(\mathbf{L}) \leq k} \|\mathbf{X} - \mathbf{L} - \mathbf{S}_{t-1}\|_F^2 \\ \mathbf{S}_t &= \arg \min_{\text{card}(\mathbf{S}) \leq rn} \|\mathbf{X} - \mathbf{L}_{t-1} - \mathbf{S}\|_F^2. \end{aligned} \quad (3)$$

The matrices \mathbf{L} and \mathbf{S} are updated alternately. Then the sparse matrix, which includes the anomaly targets, and the low-rank matrix are obtained.

B. Sparse Nonnegative Matrix Factorization

The low rank of the HSI background can be restored through several basis vectors and corresponding coefficients. The low-rank theory of the HSI background is vastly consistent with the parts-based representation theory in NMF. NMF considers that the natural signal can be stored effectively by learning a parts-based representation [23]. The general formula of NMF is

$$\mathbf{X} \approx \mathbf{W}\mathbf{H} \quad (4)$$

where \mathbf{X} is the original matrix, \mathbf{W} is the basal low-rank matrix, and \mathbf{H} is the coefficient sparse matrix.

Then, a proper objective function is needed to find the solution of the matrices \mathbf{W} and \mathbf{H} . There are two widely used objective functions [31]

$$F = \|\mathbf{X} - \mathbf{W}\mathbf{H}\|^2 = \sum \left(\mathbf{X}_{ij} - (\mathbf{W}\mathbf{H})_{ij} \right)^2 \quad (5)$$

$$P(\mathbf{X} \|\mathbf{W}\mathbf{H}) = \sum \left(\mathbf{X}_{ij} \log \frac{\mathbf{X}_{ij}}{(\mathbf{W}\mathbf{H})_{ij}} - \mathbf{X}_{ij} + (\mathbf{W}\mathbf{H})_{ij} \right) \quad (6)$$

where i and j are the row and column number of matrix \mathbf{X} , respectively.

Equation (5) measures the Euclidean distance between the original matrix and the reconstructed matrix, (6) is a variant of the Kullback–Leibler divergence that measures the similarity between matrix \mathbf{X} and matrix $\mathbf{W}\mathbf{H}$.

Then, we consider the solution of NMF as the optimization problems of two alternative formulations according to (5) and (6)

$$\min \|\mathbf{X} - \mathbf{W}\mathbf{H}\|^2$$

$$\text{s.t. } \mathbf{W} \geq 0, \mathbf{H} \geq 0 \quad (7)$$

$$\min P(\mathbf{X} \|\mathbf{W}\mathbf{H})$$

$$\text{s.t. } \mathbf{W} \geq 0, \mathbf{H} \geq 0. \quad (8)$$

Then, the multiplicative update rules of matrices \mathbf{W} and \mathbf{H} can be given by the gradient descent method

$$\mathbf{W}_{ik} \leftarrow \mathbf{W}_{ik} (\mathbf{X}\mathbf{H}^T)_{ik} / (\mathbf{W}\mathbf{H}\mathbf{H}^T)_{ik}$$

$$\mathbf{H}_{kj} \leftarrow \mathbf{H}_{kj} (\mathbf{W}^T \mathbf{X})_{kj} / (\mathbf{W}^T \mathbf{W}\mathbf{H})_{kj}$$

$$\text{s.t. } \mathbf{W} \geq 0, \mathbf{H} \geq 0 \quad (9)$$

$$\mathbf{W}_{ik} \leftarrow \left[\mathbf{W}_{ik} \sum_j (\mathbf{H}_{kj} \mathbf{X}_{ij} / (\mathbf{W}\mathbf{H})_{ij}) \right] / \sum_j \mathbf{H}_{kj}$$

$$\mathbf{H}_{kj} \leftarrow \left[\mathbf{H}_{kj} \sum_i (\mathbf{W}_{ik} \mathbf{X}_{ij} / (\mathbf{W}\mathbf{H})_{ij}) \right] / \sum_i \mathbf{W}_{ik}$$

$$\text{s.t. } \mathbf{W} \geq 0, \mathbf{H} \geq 0 \quad (10)$$

where k is the number of the basis vectors in \mathbf{W} .

The convergence of the multiplicative rules was proved in [23] and [31].

The learning speed of the basis matrix and coefficient matrix is closely related to the sparseness of the training data [15], [23]. From another perspective, controlling the number of the basis vectors in recovering each pixel of the background of HSI can reduce the redundancy and pinpoint the most accurate solution.

The SNMF selects the second objective function to ensure the completely multiplicative update rules of matrices \mathbf{W} and \mathbf{H} . Then, the cost function of SNMF [32] is defined as

$$\begin{aligned} P(\mathbf{X} \|\mathbf{W}\mathbf{H}) &= \sum \left(\mathbf{X}_{ij} \log \frac{\mathbf{X}_{ij}}{(\mathbf{W}\mathbf{H})_{ij}} - \mathbf{X}_{ij} + (\mathbf{W}\mathbf{H})_{ij} \right) \\ &+ \alpha \sum_{k,j} h_{kj} \end{aligned} \quad (11)$$

where α is the positive constant.

III. PROPOSED METHOD

A. PRLRaSAD Model for HSI

The matrix \mathbf{L} in the LRaSMD model represents the low-rank component in HSI. This model is holistic, which means that it searches the low-rank matrix solution from an overall perspective. As we know, each HSI is comprised of several different ground objects. In other words, a linear representation relationship exists between the basis vectors and each pixel in HSI [7]. The basis vectors can be viewed as all the endmembers in HSI. Taking the linear representation relationship between the basis vectors and each pixel in HSI into consideration, the model of PRLRaSAD can be described as

$$\mathbf{X} = \mathbf{B}_{i \times k} \mathbf{C}_{k \times j} + \mathbf{S}_{i \times j} + \mathbf{N}_{i \times j} \quad (12)$$

where \mathbf{X} is the two-dimensional hyperspectral matrix; i is the number of the bands and j is the number of the pixels in HSI; \mathbf{B} is the basal low-rank matrix; k is the number of the basis vectors and it can be interpreted as the number of the endmember

categories in the background; matrix C is the sparse coefficient matrix; S is the sparse matrix including the anomaly targets and N represents the noise.

The advantages of the PRLRaSAD model can be summarized as follows. First, it preserves the representation advantage of the LRaSMD model, which divides the HSI as the sum of the low-rank component, sparse component, and noise. Second, the PRLRaSAD model fully utilizes the parts-based representation and global representation. The background component has a low-rank property that is easily projected into a low-dimensional space. The potential basis structure of the background would be clearer in the low-dimensional space. Then, the background is reconstructed as the parts-based representation. The sparseness property of the anomaly target makes it difficult to store via the basis vector. Therefore, the anomaly target is modeled by a holistic representation. When we consider both the internal connection, which is between the basis vectors and each pixel in HSI, and the external connection, which is between the low rank and sparse component, the decomposition accuracy can be improved.

B. PRLRaSAD Method

Based on the description model of (12), the solution of (12) can be acquired by solving the following optimization problem:

$$\begin{aligned} \min P = & \sum \left((\mathbf{X} - \mathbf{S})_{ij} \log \frac{(\mathbf{X} - \mathbf{S})_{ij}}{(\mathbf{BC})_{ij}} - (\mathbf{X} - \mathbf{S})_{ij} \right. \\ & \left. + (\mathbf{BC})_{ij} \right) + \alpha \sum_{kj} c_{kj} \\ \text{s.t. } & \text{rank}(\mathbf{B}) \leq k, \sum_i \mathbf{B}_{ik} = 1, \text{card}(\mathbf{S}) \leq rn, \mathbf{B} \geq 0, \mathbf{C} \geq 0. \end{aligned} \quad (13)$$

In (13), there are three matrices that must be solved. The optimization problem in (13) can thus be converted into three subproblems

$$\mathbf{B}_t = \arg \min_{\text{rank}(\mathbf{B}) \leq k} P(\mathbf{B}, \mathbf{C}_{t-1}, \mathbf{S}_{t-1}) \quad (14)$$

$$\mathbf{C}_t = \arg \min P(\mathbf{B}_{t-1}, \mathbf{C}, \mathbf{S}_{t-1}) \quad (15)$$

$$\mathbf{S}_t = \arg \min_{\text{card}(\mathbf{S}) \leq rn} P(\mathbf{B}_{t-1}, \mathbf{C}_{t-1}, \mathbf{S}). \quad (16)$$

The SNMF method is employed to solve the basis matrix B and coefficient matrix C . When we solve the matrices B and C , matrix S is fixed. Then, the objective function is converted as

$$\begin{aligned} \min P = & \sum \left(\mathbf{X}'_{ij} \log \frac{\mathbf{X}'_{ij}}{(\mathbf{BC})_{ij}} - \mathbf{X}'_{ij} + (\mathbf{BC})_{ij} \right) \\ & + \alpha \sum_{kj} c_{kj} \\ \text{s.t. } & \text{rank}(\mathbf{B}) \leq k, \sum_i \mathbf{B}_{ik} = 1, \mathbf{B} \geq 0, \mathbf{C} \geq 0 \end{aligned} \quad (17)$$

where $\mathbf{X}' = \mathbf{X} - \mathbf{S}$.

When updating matrix B , matrix C is fixed. Matrix B is thus converted to

$$\begin{aligned} \mathbf{B} = \arg \min L(\mathbf{B}) = \arg \min P(\mathbf{B}, \mathbf{C}) \\ \text{s.t. } \text{rank}(\mathbf{B}) \leq k, \sum_i \mathbf{B}_{ik} = 1, \mathbf{B} \geq 0. \end{aligned} \quad (18)$$

In (18), a sum-to-one constraint is added to matrix B . This is an effective strategy to avoid the invariance of three matrices during the update process.

Followed by Lee and Seung [31], we define the auxiliary function to solve (18)

$$\begin{aligned} G(\mathbf{B}, \mathbf{B}') = & \sum_{i,j} (x'_{ij} \log x'_{ij} - x'_{ij}) \\ & + \sum_{ij} (\mathbf{BC})_{ij} - \sum_{i,j,k} x'_{ij} \frac{b'_{ik} c_{kj}}{\sum_{il} b'_{il} c_{lj}} (\log(b_{ik} c_{kj}) \\ & - \log \frac{b'_{ik} c_{kj}}{\sum_{il} b'_{il} c_{lj}}) + \alpha \sum_{k,j} c_{kj} \end{aligned} \quad (19)$$

where b'_{ik} and B' are the results of the previous step.

The auxiliary function has the following properties: $G(\mathbf{B}, \mathbf{B}) = L(\mathbf{B})$ and $G(\mathbf{B}, \mathbf{B}') \geq L(\mathbf{B})$ [23]. Then the auxiliary function can be seen as the upper bound of function $L(\mathbf{B})$. We minimize the auxiliary function to solve (18) and the update rule of matrix B is expressed as follows:

$$\mathbf{B}_{t+1} = \arg \min_{\mathbf{C}} G(\mathbf{B}, \mathbf{B}'). \quad (20)$$

Then, matrix B can be solved by $\partial G(\mathbf{B}, \mathbf{B}') / \partial b_{ik} = 0$. The update rule of matrix C can be solved through the same method. Finally, the completely multiplicative update rules of matrix B and C are as follows:

$$\begin{aligned} \mathbf{B}_{ik} & \leftarrow \left[\mathbf{B}_{ik} \sum_j (\mathbf{C}_{kj} \mathbf{X}'_{ij} / (\mathbf{BC})_{ij}) \right] / \sum_j \mathbf{C}_{kj} \\ \mathbf{B}_{ik} & \leftarrow \frac{\mathbf{B}_{ik}}{\sum_i \mathbf{B}_{ik}} \\ \mathbf{C}_{kj} & \leftarrow \left[\mathbf{C}_{kj} \sum_i (\mathbf{B}_{ik} \mathbf{X}'_{ij} / (\mathbf{BC})_{ij}) \right] / (1 + \alpha). \end{aligned} \quad (21)$$

The subproblems (14) and (15) can be solved by (21). Then, the matrix S can be updated according to

$$\mathbf{S}_t = P_{\Omega}(\mathbf{X} - \mathbf{B}_{t-1} \mathbf{C}_{t-1}) \quad (22)$$

where Ω is the first m largest nonzero vectors in $|\mathbf{X} - \mathbf{B}_{t-1} \mathbf{C}_{t-1}|$ and P_{Ω} implements the projection of matrix S onto Ω .

The final update rules of the entire solution for the PRLRaSMD method combine (21) and (22). Three matrices are updated alternately.

After obtaining the sparse matrix S , the PRLRaSAD detector can be defined as:

$$D_{\text{PRLRaSAD}} = \|\mathbf{S}_{i \times j}\|_2. \quad (23)$$

Algorithm 1: Parts Representation-Based LRaSMD Anomaly Target Detector.

Input: a) $X \in \mathbb{R}^{b \times n}$, the two-dimensional HSI matrix
b) k , the maximal rank number of matrix B
c) r , the cardinality of matrix S
d) t , the iteration number

Output: a) B , approximation of the basis vector matrix
b) C , approximation of the coefficient matrix
c) S , approximation of the sparse component
d) D_{PRLRaSAD} , the detection result of the PRLRaSAD detector

Procedure (1) **Initialize:** a) $B_0 \leftarrow$ using RXD
b) $C_0, S_0 \leftarrow$ calculated by (24)
2) $\alpha \leftarrow$ calculated by (26)
3) **while** (1)
4) update the matrices B_i, C_i, S_i by (21) and
(22)
5) **if** $i \geq t$
6) **break**
7) **end if**
8) **end while**
9) **return** B, C, S
10) $D_{\text{PRLRaSAD}} \leftarrow$ calculated by (23)

The anomaly target prominently shows a large value in the results.

The procedure of PRLRaSAD is shown in Algorithm 1.

C. Initialization and Termination Condition

In the traditional LRaSMD-based and NMF-based algorithms, the initialization of the matrices B , C , and S is selected as random. However, the random initialization may lead to extremely uncertain factorization results, which could subsequently affect the performance of the proposed detector randomly.

In the proposed method, we use the global RXD detector to initialize the basis vectors in matrix B . The pixel vectors in the original HSI, which have the small corresponding values in the RXD result, are selected to compose the initialized matrix B . Then, matrices C and S can be initialized as

$$\begin{aligned} C &= (B^T B)^{-1} B^T X \\ S &= X - BC. \end{aligned} \quad (24)$$

The accuracy of matrix S has a close relationship with matrices B and C . Therefore, we can use the empirical method in the NMF-based algorithms to terminate the update process of the three matrices.

Lee and Seung [23] have proved that the original NMF algorithm, which uses the random method to initialize matrices B and C , can mostly converge after 50 iterations. The iteration number was set to 500 in the experiments of that study. In many NMF-based algorithms, the iteration number ranges from 10 to 200 [31], [32]. Therefore, the iteration number used in the following experiments was set to 100. Since the initialization

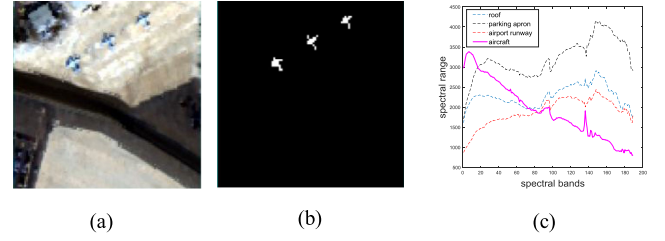


Fig. 1. (a) San Diego scene. (b) Location of anomaly targets. (c) Spectra of main materials in the San Diego scene.

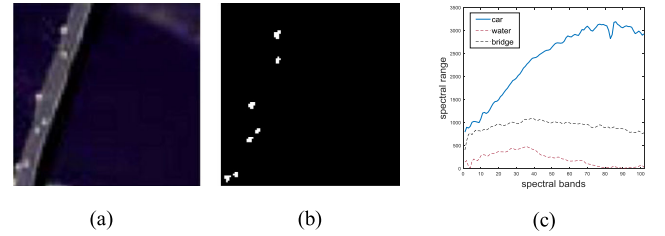


Fig. 2. (a) PaviaC scene. (b) Location of anomaly targets. (c) Spectra of main materials in the PaviaC scene.

method is more stable than the traditional NMF-based algorithms, 100 iterations are enough to achieve the stable factorization results for matrices B and C .

IV. EXPERIMENTAL RESULTS

A. Hyperspectral Data

Five data sets were utilized to verify the effectiveness of the proposed method, including San Diego, PaviaC, Texas coast, pushbroom hyperspectral imager (PHI), and Cri data sets.

The first data set is shown in Fig. 1(a) with the size of 100×100 pixels. The corresponding ground truth location is shown in Fig. 1(b). The San Diego airport data set was acquired by the airborne visible/infrared imaging spectrometer (AVIRIS) sensor. The San Diego data set has 189 effective spectral channels and excluded a low signal to noise ratios or other bad bands. The wavelength ranged from 370 to 2510 nm. Three white aircraft were selected as intended anomaly targets. The spectra of the main ground objects are shown in Fig. 1(c).

The second data collection is a part of Pavia Centre and University data set (referred to as the PaviaC data set) covering an area of 105×105 pixels, as shown in Fig. 2(a). It was collected by the reflective optics system imaging spectrometer sensor. The ground truth of the anomaly target in the PaviaC scene is shown in Fig. 2(b). The PaviaC scene is mainly composed of water, bridge, and several cars. The spectra of the cars are distinctly different from the other ground objects, and thus, the cars are the intended anomaly targets. The spectra of the main ground objects are shown in Fig. 2(c).

The third data set is one of the ABU data set [34], with a size of 100×100 pixels, and is shown in Fig. 3(a). This data set was captured by the AVIRIS sensor at the Texas coast. The ground truth of the Texas coast scene is depicted in Fig. 3(b). The main ground object in the Texas coast scene is the vegetation. The spectra of the main ground objects are shown in Fig. 3(c).

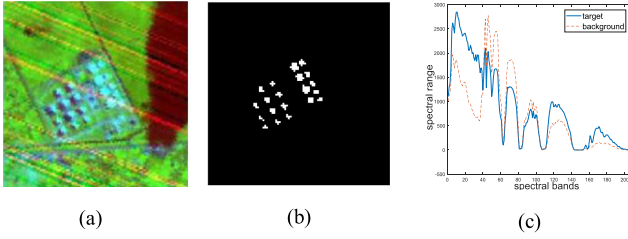


Fig. 3. (a) Texas coast scene. (b) Location of anomaly targets. (c) Spectra of main materials in the Texas coast scene.

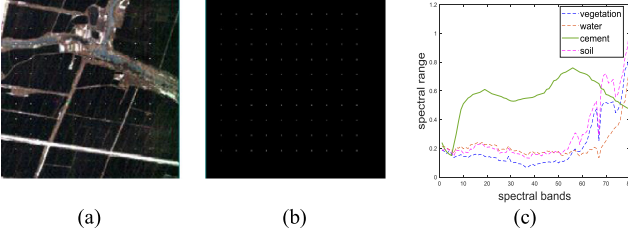


Fig. 4. (a) PHI scene. (b) Location of anomaly targets. (c) Spectra of main materials in the PHI scene.

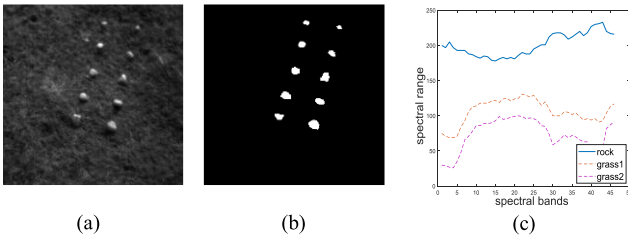


Fig. 5. (a) Cri scene. (b) Location of anomaly targets. (c) Spectra of main materials in the Cri scene.

The fourth data set was acquired by the PHI with a size of 240×240 pixels [as shown in Fig. 4(a)]. In the PHI scene, 100 cement pixels with different abundances were embedded. The anomaly targets in the first row were comprised of 90% background and 10% cement. The remaining targets followed the rule that the background decreased by 10% per row and the cement increased by 10% per row. The locations of the anomaly targets and the spectra of the main materials in the PHI scene are depicted in Fig. 4(b) and (c).

The fifth data set is shown in Fig. 5(a) with a size of 400×400 pixels and was collected by the Nuance Cri imaging spectrometer. It is mainly composed of grass and ten rocks. Compared with the grass, the spectra of the rocks are distinctly different. Thus, the rocks were considered as the intended anomaly targets. The locations of the anomaly targets and the spectra of the main materials in the Cri scene were depicted in Fig. 5(b) and (c).

B. Experimental Results and Discussion

1) *Parameter Analysis*: There are three important parameters in the proposed method. They are positive constant coefficient α , the number of basis vectors k , and sparsity parameter r . Since the positive constant α determines the weight

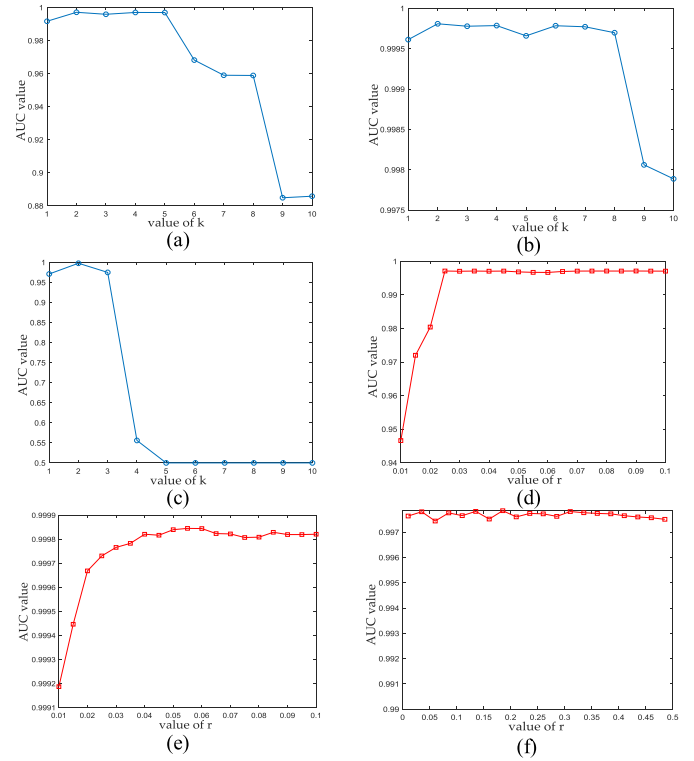


Fig. 6. AUC values of PRLRaSAD with respect to different k for (a) San Diego, (b) PaviaC, and (c) Texas coast. AUC values of PRLRaSAD with respect to different r for (d) San Diego, (e) PaviaC, and (f) Texas coast.

of the sparseness constraint term in solving the matrices B and C , the value of α should be set according to the specific situation. In [35], a sparse code model is proposed as follows:

$$E = - [\text{preserve information}] - \lambda [\text{sparseness constrain on coefficient}] \quad (25)$$

where λ is the positive constant, which has the same meaning of α .

The value of λ is determined by $\lambda/\sigma = 0.14$, where σ is the standard deviation. The values of α and λ are related to the discreteness of the original HSI. Therefore, the value of α in the following experiments is determined by:

$$\alpha = \frac{\sum \text{norm}(\mathbf{X}_1(i) - \text{mean_X})}{n - 1} \quad (26)$$

where mean_X is the mean vector of the normalized HSI and $\mathbf{X}_1(i)$ is the normalized vector of the original pixels in the HSI.

The remaining parameters are the number of basis vectors k and sparsity parameter r . To explore the value setting of k and r , we designed a group of experiments, in which k and r were set to different values. These experiments utilized the San Diego, PaviaC, and Texas coast data sets. In this section, a detection performance criterion AUC was used. A detailed explanation of AUC is introduced in Section IV-B3.

The AUC values in Fig. 6 show the performances of PRLRaSAD with respect to k and r . For the San Diego data set, PRLRaSAD performed the best when k was set to 5 and the

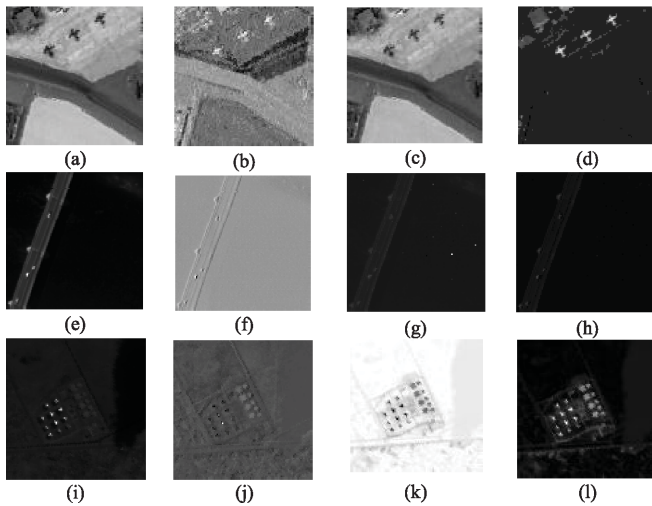


Fig. 7. (a) Low rank and (b) sparse component acquired by LRaSMD. (c) Low rank and (d) sparse component acquired by PRLRaSAD in the San Diego scene. (e) Low rank and (f) sparse component acquired by LRaSMD. (g) Low rank and (h) sparse component acquired by PRLRaSAD in the PaviaC scene. (i) Low rank and (j) sparse component acquired by LRaSMD. (k) Low rank and (l) sparse component acquired by PRLRaSAD in the Texas coast scene.

detection ability of PRLRaSAD was stable when k was less than 5. When k was greater than 5, the AUC value rapidly decreased. For the PaviaC data set, the AUC value reached its maximum when k was set to 2 and then maintained a stable detection performance. Conversely, AUC decreased when k was greater than 8. For the Texas coast scene, the AUC value of PRLRaSAD reached its maximum when k was set to 2. Then, the AUC value decreased suddenly. The above-mentioned analysis demonstrated that k was generally set to a small value. Similar conclusions were drawn in [14], [20], and so on.

Interestingly, the k value has a positive correlation with the number of the main ground objects in the original HSI. The San Diego scene contained more objects than the other two data sets. As a result, the k value used in the San Diego scene was greater than the other two data sets. A weak empirical approach can be used in setting the parameter k to the number of the main materials in the original HSI.

Sparsity parameter r is related to the ratio of the anomaly targets in HSI [14]. Fig. 6 demonstrates that the detection performance was more stable when r was set to different values. Thus, it is reasonable to set an r range of 0.05–0.1. Therefore, r was set to 0.05, 0.06, and 0.05 for the San Diego, PaviaC, and Texas coast data, respectively.

2) *Effectiveness of Decomposition Evaluation*: In this section, we design a group of experiments to intuitively show the decomposition effectiveness of the low rank and sparse component. Fig. 7 shows the decomposition result of the low rank and sparse component of HSI utilizing LRaSMD and the improved LRaSMD in PRLRaSAD, respectively. These images both select the 100th band of the low rank and sparse component.

From Fig. 7, we can find that the background and anomaly target are not separated very well using the original LRaSMD method. For example, some background information still remains in the sparse component in Fig. 7(a) and the situation in

TABLE I
AUC VALUES OF NINE ALGORITHMS IMPLEMENTED FOR FIVE DATA SETS

Methods	Datasets				
	San Diego	PaviaC	Texas coast	PHI	Cri
RXD	0.9077	0.9947	0.9861	0.9081	0.9069
KRXD	0.9563	0.9267	0.9613	0.8944	0.7425
SSRX	0.9942	0.8095	0.9538	0.9565	0.9701
CRD	0.9200	0.9736	0.9793	0.9091	0.9752
BACON	0.8975	0.9954	0.8664	0.8912	0.8977
EDLRaSMD	0.9834	0.9916	0.9854	0.9698	0.9589
LSDRAD	0.9914	0.9843	0.9929	0.9265	0.9674
SC-CNMF based detector	0.9857	0.9783	0.9802	0.9381	0.9785
PRLRaSAD	0.9972	0.9998	0.9977	0.9856	0.9846

Fig. 7(d) can be better. The same situation exists in the other two data sets.

3) *Detection Performance Evaluation*: In this section, some traditional anomaly target detection algorithms are used for a comparison purpose, including global RXD [10], kernel RXD [36], SSRXD [13], collaborative representation detector [37], LSDRAD [21], SC-CNMF anomaly detector [27], BACON [12], and EDLRaSMD [20]. Then, the eight comparative algorithms and the PRLRaSAD were implemented for the five data sets. Finally, we chose three widely used evaluation criteria to evaluate the performances of nine algorithms: receiver operating characteristic (ROC), area under ROC curve (AUC), and target-background separability map.

In the EDLRaSMD and LSDRAD, the rank number setting of the low-rank matrix is set using the empirical approach mentioned in Section IV-B1.

The lateral axis of the ROC curve is the false alarm rate and the vertical axis is the detection rate. The ROC curve intuitively depicts the detection performances of nine algorithms under the same false alarm rate. When two ROC curves intersect, it is difficult to observe the detection performance. Then, the AUC value can be used to further evaluate the performance. The AUC value is the area under the ROC curve and its maximum value is 1. The closer the AUC is to 1, the better the detector performance is.

The AUC values of nine algorithms are depicted in Table I. We can find that the proposed method achieved a superior performance compared with the other eight traditional algorithms and it maintained a stable detection performance in all five data sets. This result shows that the PRLRaSMD has distinct advantages in describing HSI compared with the traditional algorithms. Additionally, the proposed method also improved the accuracy of the low rank and sparse components.

The ROC curves of all algorithms implemented for five data sets are shown in Fig. 8. The results show that the proposed algorithm outperformed the other algorithms. The proposed method achieved a detection rate over 99% and controlled the false alarm rate under 1% in five data sets. Especially PaviaC and

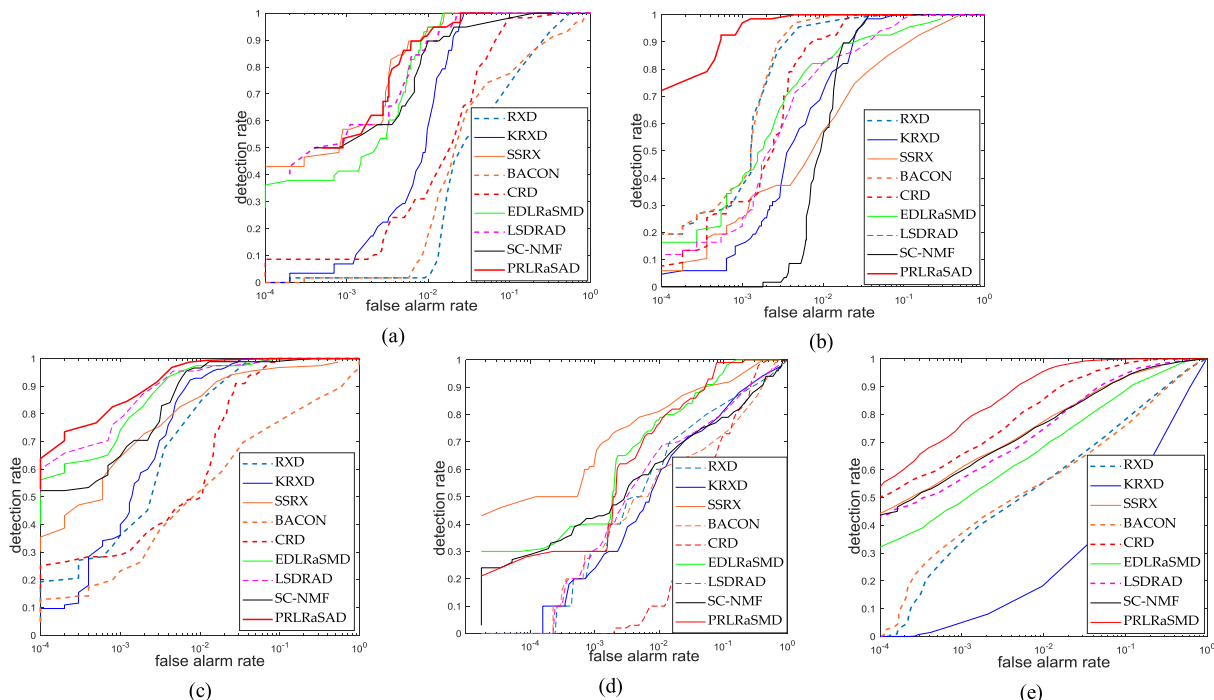


Fig. 8. ROC curves of five algorithms implemented on (a) San Diego scene, (b) PaviaC scene, (c) Texas coast scene, (d) PHI scene, and (e) Cri scene.

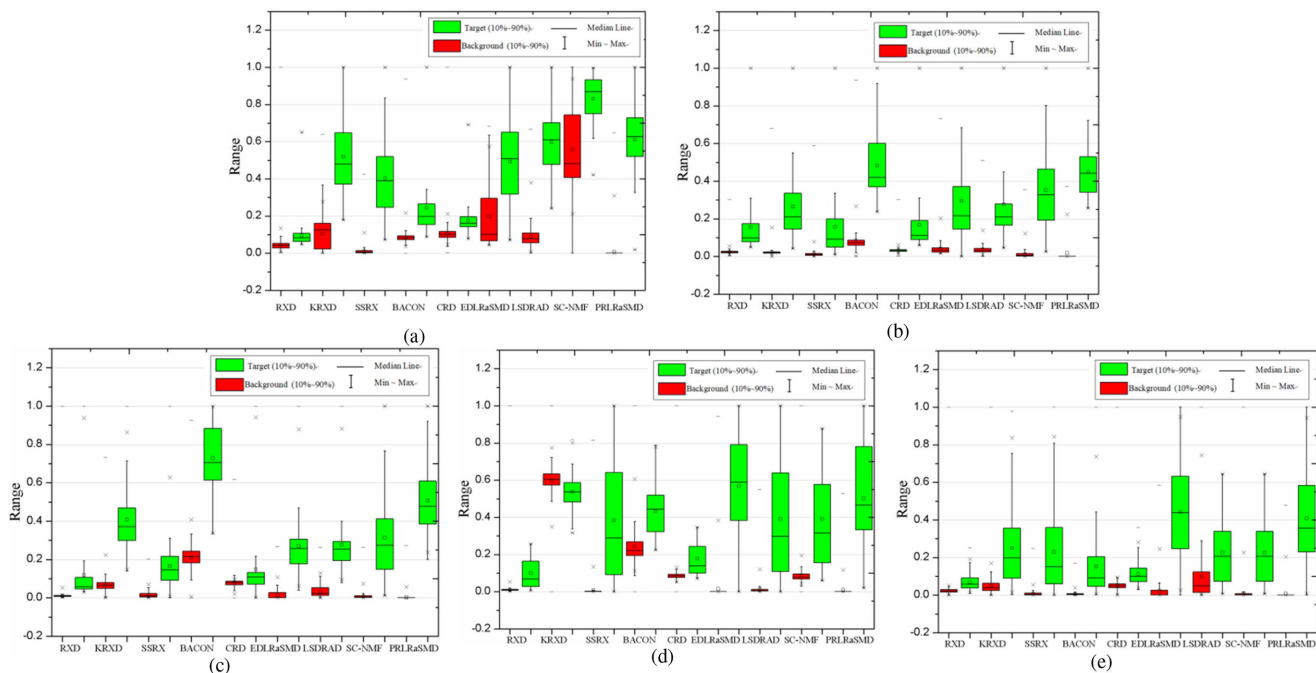


Fig. 9. Separability maps of five algorithms implemented on (a) San Diego scene, (b) PaviaC scene, (c) Texas coast scene, (d) PHI scene, and (e) Cri scene.

Cri scenes in which the background are simple, the advantages of the parts-based representation in the proposed method are obvious.

Since the separation degree between the anomaly target and background also is an important index for evaluating the performance of the detector, the separability maps of all algorithms

were created for experiments. There are two boxes in each separability map. As shown in Fig. 9, the green box represents the distribution of the targets statistical detection values and the red box is the distribution of the background detection statistic values. The distance between the two boxes reveals the separation degree between the target and background. The farther the

distance is, the higher the separation degree between the target and background is.

The separability maps of nine methods implemented on five datasets are depicted in Fig. 9. Fig. 9 shows that the red boxes for the proposed method in the five separability maps are shorter than in the other methods. This demonstrates that the proposed method achieved a superior performance in suppressing the background information. In addition, the distance between the red box and green box of the proposed method is also farther than that in the other methods. These results also prove that the proposed method can separate the target and background more effectively.

We, therefore, conclude that the model in our proposed method can describe the background more effectively than the traditional model. Finally, the anomaly target detection ability of the PRLRaSAD was further improved.

V. CONCLUSION

In this article, we proposed a novel anomaly target detection algorithm that improved the original LRaSMD algorithms to obtain a more accurate decomposition of HSI. The advantage of the proposed method was that it combines the parts-based and holistic-based representation to model the original HSI. The background was based on the parts-based representation. The anomaly target was based on a holistic-based representation due to its sparse properties. Based on the above-mentioned description of HSI, the proposed method divides the HSI decomposition optimization problem into three subproblems to compute the basis vector matrix, coefficient matrix, and sparse matrix, respectively. In both the original and improved LRaSMD, the accuracy of the sparse component was closely related to the accuracy of the low-rank component. Therefore, we introduced the SNMF to assist in solving the low-rank component and further improved the accuracy of the sparse component. Finally, the basis vector matrix, coefficient matrix, and sparse matrix were solved by new update rules. Since the anomaly targets existed in the sparse component, the sparse matrix was thus employed to implement the anomaly detection. Extensive experiments clearly show that the proposed method achieved a superior detection performance.

REFERENCES

- [1] Q. Tong, B. Zhang, and L. Zhang, "Current progress of hyperspectral remote sensing in China," *J. Remote Sens.*, vol. 20, no. 5, pp. 689–707, Sep. 2016.
- [2] L. Zhang, L. Zhang, B. Du, J. You, and D. Tao, "Hyperspectral image unsupervised classification by robust manifold matrix factorization," *Inf. Sci.*, vol. 485, pp. 154–169, Jun. 2019.
- [3] J. M. Bioucas-Dias, A. Plaza, G. Camps-Valls, P. Scheunders, N. Nasrabadi, and J. Chanussot, "Hyperspectral remote sensing data analysis and future challenges," *IEEE Geosci. Remote Sens. Mag.*, vol. 1, no. 2, pp. 6–36, Jun. 2013.
- [4] R. Tao, X. Zhao, W. Li, H.-C. Li, and Q. Du, "Hyperspectral anomaly detection by fractional fourier entropy," *IEEE J. Sel. Topics Appl. Earth Observ. Remote Sens.*, vol. 12, no. 12, pp. 4920–4929, Dec. 2019.
- [5] W. Sun, L. Tian, Y. Xu, B. Du, and Q. Du, "A randomized subspace learning based anomaly detector for hyperspectral imagery," *Remote Sens.*, vol. 10, no. 3, p. 417, Mar. 2018.
- [6] Y. Zhang, K. Wu, B. Du, and X. Hu, "Regularization framework for target detection in hyperspectral imagery," *IEEE J. Sel. Topics Appl. Earth Observ. Remote Sens.*, vol. 12, no. 7, pp. 2135–2147, Jul. 2019.
- [7] F. C. Robey, D. R. Fuhrmann, E. J. Kelly, and R. Nitzberg, "A CFAR adaptive matched filter detector," *IEEE Trans. Aerosp. Electron. Syst.*, vol. 28, no. 1, pp. 208–216, Jan. 1992.
- [8] X. Zhang and P. Li, "Lithological mapping from hyperspectral data by improved use of spectral angle mapper," *Int. J. Appl. Earth Observ. Geoinf.*, vol. 31, pp. 95–109, 2014.
- [9] H. Kwon and N. M. Nasrabadi, "Hyperspectral target detection using kernel orthogonal subspace projection," in *Proc. IEEE Int. Conf. Image Process.*, Genova, Italy, 2005, pp. 1–4.
- [10] I. S. Reed and X. Yu, "Adaptive multiple-band CFAR detection of an optical pattern with unknown spectral distribution," *IEEE Trans. Acoust. Speech, Signal Process.*, vol. 38, no. 10, pp. 1760–1770, Oct. 1990.
- [11] Y. P. Taitano, B. A. Geier, and K. W. Bauer, "A locally adaptable iterative RX detector," *Eurasip J. Adv. Signal Process.*, vol. 2010, no. 1, Jan. 2010, Art. no. 341908.
- [12] N. Billor, A. S. Hadi, and P. F. Velleman, "BACON: Blocked adaptive computationally efficient outlier nominators," *Comput. Statistics Data Anal.*, vol. 34, no. 3, pp. 279–298, Sep. 2000.
- [13] A. P. Schaum, "Hyperspectral anomaly detection beyond RX," *Proc. SPIE*, vol. 6565, no. 656502, pp. 1–4, May 2007.
- [14] Y. Zhang, B. Du, L. Zhang, and S. Wang, "A low-rank and sparse matrix decomposition-based mahalanobis distance method for hyperspectral anomaly detection," *IEEE Trans. Geosci. Remote Sens.*, vol. 54, no. 3, pp. 1376–1389, Mar. 2016.
- [15] Y. Chen, N. M. Nasrabadi, and T. D. Tran, "Hyperspectral image classification via kernel sparse representation," *IEEE Trans. Geosci. Remote Sens.*, vol. 51, no. 1, pp. 217–231, Jan. 2013.
- [16] Y. Xu, Z. Wu, J. Li, A. Plaza, and Z. Wei, "Anomaly detection in hyperspectral images based on low-rank and sparse representation," *IEEE Trans. Geosci. Remote Sens.*, vol. 54, no. 4, pp. 1990–2000, Nov. 2016.
- [17] Y. Zhang, B. Du, L. Zhang, and T. Liu, "Joint sparse representation and multitask learning for hyperspectral target detection," *IEEE Trans. Geosci. Remote Sens.*, vol. 55, no. 2, pp. 894–906, Feb. 2017.
- [18] Y. Dong, B. Du, and L. Zhang, "Target detection based on random forest metric learning," *IEEE J. Sel. Topics Appl. Earth Observ. Remote Sens.*, vol. 8, no. 4, pp. 1830–1838, Apr. 2015.
- [19] X. Cui, Y. Tian, L. Weng, and Y. Yang, "Anomaly detection in hyperspectral imagery based on low-rank and sparse decomposition," in *Proc. Int. Conf. Graphic Image Process.*, Hongkong, China, 2014, pp. 1–7.
- [20] W. Sun, C. Liu, J. Li, Y. M. Lai, and W. Li, "Low-rank and sparse matrix decomposition-based anomaly detection for hyperspectral imagery," *J. Appl. Remote Sens.*, vol. 8, no. 1, May 2014, Art. no. 083641.
- [21] Y. Xu, B. Du, L. Zhang, and S. Chang, "A low-rank and sparse matrix decomposition-based dictionary reconstruction and anomaly extraction framework for hyperspectral anomaly detection," *IEEE Geosci. Remote Sens. Lett.*, to be published, doi: 10.1109/LGRS.2019.2943861.
- [22] F. K uc uk, B. U. T oreyin, and F. V.  elebi, "Sparse and low-rank matrix decomposition-based method for hyperspectral anomaly detection," *J. Appl. Remote Sens.*, vol. 13, no. 1, 2019, Art. no. 014519.
- [23] D. D. Lee and H. S. Seung, "Learning the parts of objects by non-negative matrix factorization," *Nature*, vol. 401, no. 6755, pp. 788–791, Oct. 1999.
- [24] Y. Liu and F.-B. Zheng, "Object-oriented and multi-scale target classification and recognition based on hierarchical ensemble learning," *Comput. Elect. Eng.*, vol. 62, pp. 538–554, Aug. 2017.
- [25] X. Long, H. Lu, P. Yong, and W. Li, "Graph regularized discriminative non-negative matrix factorization for face recognition," *Multimedia Tools Appl.*, vol. 72, no. 3, pp. 2679–2699, Oct. 2014.
- [26] N. Wang, B. Du, and L. Zhang, "An endmember dissimilarity constrained non-negative matrix factorization method for hyperspectral unmixing," *IEEE J. Sel. Topics Appl. Earth Observ. Remote Sens.*, vol. 6, no. 2, pp. 554–569, Apr. 2013.
- [27] W. Zhang, X. Lu, and X. Li, "Similarity constrained convex nonnegative matrix factorization for hyperspectral anomaly detection," *IEEE Trans. Geosci. Remote Sens.*, vol. 57, no. 7, pp. 4810–4822, Jul. 2019.
- [28] P. O. Hoyer, "Modeling receptive fields with non-negative sparse coding," *Neurocomputing*, vol. 52/54, no. 02, pp. 547–552, Jun. 2003.
- [29] Z. Yang and E. Oja, "Linear and nonlinear projective nonnegative matrix factorization," *IEEE Trans. Neural Netw.*, vol. 21, no. 5, pp. 734–749, May 2010.
- [30] H. Zhang, W. He, L. Zhang, H. Shen, and Q. Yuan, "Hyperspectral image restoration using low-rank matrix recovery," *IEEE Trans. Geosci. Remote Sens.*, vol. 52, no. 8, pp. 4729–4743, Aug. 2014.
- [31] D. D. Lee and H. S. Seung, "Algorithms for non-negative matrix factorization," *Adv. Neural Inf. Process. Syst.*, vol. 13, pp. 556–562, Feb. 2001.

- [32] W. Liu, N. Zheng, and X. Lu, "Non-negative matrix factorization for visual coding," in *Proc. Int. Conf. Acoust., Speech, Signal Process.*, Hong Kong, China, 2003, pp. 293–296.
- [33] L. Ji, X. Geng, K. Yu, and Y. Zhao, "A new non-negative matrix factorization method based on barycentric coordinates for endmember extraction in hyperspectral remote sensing," *Int. J. Remote Sens.*, vol. 34, no. 19, pp. 6577–6586, Oct. 2013.
- [34] X. Kang, X. Zhang, S. Li, K. Li, and J. A. Benediktsson, "Hyperspectral anomaly detection with attribute and edge-preserving filters," *IEEE Trans. Geosci. Remote Sens.*, vol. 55, no. 10, pp. 5600–5611, Oct. 2017.
- [35] B. A. Olshausen and D. J. Field, "Emergence of simple-cell receptive field properties by learning a sparse code for natural images," *Nature*, vol. 381, no. 6583, pp. 607–609, Jul. 1996.
- [36] H. Kwon and N. M. Nasrabadi, "Kernel RX-algorithm: A nonlinear anomaly detector for hyperspectral imagery," *IEEE Trans. Geosci. Remote Sens.*, vol. 43, no. 2, pp. 388–397, Feb. 2005.
- [37] W. Li and Q. Du, "Collaborative representation for hyperspectral anomaly detection," *IEEE Trans. Geosci. Remote Sens.*, vol. 53, no. 3, pp. 1463–1474, Mar. 2015.



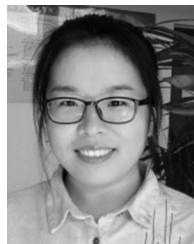
Yan Zhang received the B.E. degree in remote sensing science and technology from the Shandong University of Science and Technology, Qingdao, China, in 2017. She is currently working toward the M.S. degree in photogrammetry and remote sensing with the College of Oceanography and Space Informatics, China University of Petroleum (East China), Qingdao, China.

Her current research interests include hyperspectral target detection and anomaly target detection.



Yanguo Fan received the B.S. and M.S. degrees in engineering survey from Wuhan University, Wuhan, China, in 1992 and 1998, respectively, and the Ph.D. degree in cartography and geographic information engineering from the China University of Mining and Technology, Beijing, China, in 2007.

He is currently a Professor with the College of Oceanography and Space Informatics, China University of Petroleum (East China), Qingdao, China. His research interests are on land information and land planning, and hyperspectral imagery processing.



Mingming Xu (Member, IEEE) received the B.S. degree in surveying and mapping engineering from the China University of Petroleum, Beijing, China, in 2011, and the Ph.D. degree in photogrammetry and remote sensing from the State Key Lab of Information Engineering in Surveying, Mapping, and Remote Sensing, Wuhan University, Wuhan, China, in 2016.

She is currently a Lecturer with the College of Oceanography and Space Informatics, China University of Petroleum, Beijing, China. Her major research interests include hyperspectral image processing and intelligent computation.



Wei Li (Senior Member, IEEE) received the B.E. degree in telecommunications engineering from Xidian University, Xi'an, China, in 2007, the M.S. degree in information science and technology from Sun Yat-Sen University, Guangzhou, China, in 2009, and the Ph.D. degree in electrical and computer engineering from Mississippi State University, Starkville, MS, USA, in 2012.

Subsequently, he spent one year as a Postdoctoral Researcher with the University of California, Davis, CA, USA. He is currently a Professor with the School

of Information and Electronics, Beijing Institute of Technology, Beijing, China. His current research interests include hyperspectral image analysis, pattern recognition, and data compression.

Prof. Li is an active Reviewer for the IEEE TRANSACTIONS ON GEOSCIENCE AND REMOTE SENSING, the IEEE GEOSCIENCE REMOTE SENSING LETTERS, and the IEEE JOURNAL OF SELECTED TOPICS IN APPLIED EARTH OBSERVATIONS AND REMOTE SENSING (JSTARS). He was the Guest Editor for Special Issue of the *Journal of Real-Time Image Processing, Remote Sensing* and IEEE JSTARS, and is currently an Associate Editor for both the IEEE SIGNAL PROCESSING LETTERS and the IEEE JSTARS. He was the recipient of the 2015 Best Reviewer Award from the IEEE Geoscience and Remote Sensing Society for his service for IEEE JSTARS.



Guangyu Zhang received the B.E. degree in spatial information and digital technology from Shandong Agricultural University, Tai'an, China, in 2017. She is currently working toward the M.S. degree in photogrammetry and remote sensing, with the College of Oceanography and Space Informatics, China University of Petroleum (East China), Qingdao, China.

Her current research interests include ocean remote sensing and hyperspectral imagery processing.

Li Liu, biography not available at the time of publication.

Dingfeng Yu, biography not available at the time of publication.